Solar Energy Materials & Solar Cells 218 (2020) 110812

Contents lists available at ScienceDirect

Solar Energy Materials and Solar Cells

journal homepage: http://www.elsevier.com/locate/solmat

High-temperature solar-selective coatings based on Cr(Al)N. Part 2: Design, spectral properties and thermal stability of multilayer stacks

T.C. Rojas [a,*], A. Caro [a], R. Escobar-Galindo [b], J.C. Sánchez-López [a]

[a] Instituto de Ciencia de Materiales de Sevilla (CSIC-Univ. Sevilla), Avda. Américo Vespucio 49, 41092, Sevilla, Spain
[b] Departamento de Física Aplicada I, Escuela Politécnica Superior, Universidad de Sevilla, Virgen de África 7, 41011, Sevilla, Spain

ARTICLE INFO

Keywords:
Solar selective absorber
CrAlN-based films
Optical simulation
High temperature
Solar absorptance
Thermal emittance

ABSTRACT

Two multilayer solar selective absorber coatings [Al/$CrN_{0.95}$/$Cr_{0.96}Al_{0.04}N_{1.08}$/$Cr_{0.53}Al_{0.47}N_{1.12}$/$Al_2O_3$ (stack #1) and $Cr_{0.96}Al_{0.04}N_{0.89}$/$Cr_{0.62}Al_{0.38}N_{1.00}$/$Cr_{0.53}Al_{0.47}N_{1.12}$/$Al_2O_3$ (stack #2)] were deposited on 316L steel by combining direct current (DC) and high power impulse magnetron sputtering (HiPIMS) technologies with the aim of increasing the working limit temperature. The composition and thickness of the constituent layers were optimized using CODE software to achieve a high solar absorptance (α) and low values of thermal emittance (ε) in the infrared region. The deposited multilayered stacks were heated during 2 h in air at 600, 700 and 800 °C to study their thermal stability and optical performance. Compositional, structural and optical characterization of the stacks (as-prepared and after thermal treatment) was performed. Both stacks presented a good solar selectivity with $\alpha > 95\%$ and $\varepsilon < 15\%$, were stable up to 600 °C and fulfilled the performance criterion PC < 5% after 600 and 700 °C treatments. Despite the stacks suffered chemical transformations above 600 °C, partial oxidation (stack #1) and Cr_2N formation (stack #1 and #2), the optical properties were optimum up to 700 °C for stack #1 ($\alpha = 94\%$, $\varepsilon_{(25\ °C)} = 12\%$) and 600 °C for stack #2 ($\alpha = 93\%$, $\varepsilon_{(25\ °C)} = 13\%$). The solar-to-mechanical energy conversion efficiencies (η) of the as-deposited and annealed (600 and 700 °C) samples were up to 20% points higher than the absorber paint commercially used (Pyromark). At 800 °C, they underwent a further structural transformation, provoked by the oxidation of the inner layers, and they consequently lost their solar selectivity.

1. Introduction

In recent years, renewable sources of energy have become a crucial issue due to the depletion of fossil fuels, increasing concentration of greenhouse gases and climate changes. In order to reduce greenhouse gases, we need to use renewable energy sources. The estimated share of renewables in global electricity generation was more than 26% by the end of 2018, and solar energy is one of the most environmentally safe energy sources. Nevertheless, solar energy production still only accounts for less than 3% and faces challenges in achieving a larger share of the global total [1]. To foster this technology, particularly in relation to concentrated solar power (CSP), a rapid development of novel materials and innovative engineering solutions are urgently needed. CSP technology harnesses the sun's power to generate electricity through thermal conversion. A heat collector element receives a concentrated radiation flux reflected from a heliostats field. Nowadays, the two most prominent commercial CSP technologies are parabolic through (PT) collectors and central receiver solar tower plants.

In the last decades, a big effort has been done to develop solar selective coatings (SSC) with high values for solar absorptance (α) in the UV–Vis region and low values of thermal emittance (ε) in the infrared (typically $\alpha > 95\%$, $\varepsilon_{25\ °C} < 15\%$) to improve the performance of the CSP receivers [2,3]. Furthermore, the coatings also need to be chemically and structurally stable within the range of operating temperatures (up to ~500 °C in vacuum for linear systems and ~800 °C or more in air for point focus systems); durable (ideally 25 years) and with good adhesion to the absorber tube [2]. It is also known that increasing competitiveness can be obtained together with an increment of the efficiency of the thermodynamic cycle using higher temperatures but this is limited by the durability of the absorber material and the working fluid (synthetic oil (400 °C), molten salts (500–565 °C)) [4]. In addition, those absorbers exposed to ambient conditions (solar tower) should be ideally oxidation- and abrasion-resistant, although it is also advised for PT collectors in the case the vacuum is ever breached.

For high-temperature applications, commercial silicone-based paints like Pyromark®-2500 and SOLKOTE® are commonly employed

* Corresponding author.
E-mail address: tcrojas@icmse.csic.es (T.C. Rojas).

https://doi.org/10.1016/j.solmat.2020.110812
Received 3 June 2020; Received in revised form 17 September 2020; Accepted 21 September 2020
Available online 1 October 2020

absorbers in solar tower technology and parabolic through collectors, respectively. However, Pyromak has poor solar selectivity (due to high thermal losses in the IR) and the optical properties suffer a fast degradation during operation above 700 °C [5] requiring permanent maintenance and reparation typically every two years. Meanwhile SOLKOTE is only thermally stable up to 538 °C and must be properly cured for glazed and vacuum applications at high temperature [6]. These facts underline the needs of development of novel SSC with high temperature stability in oxidizing atmosphere.

In recent years, transition-metal nitrides, oxides and oxynitrides have received significant attention for use in mid- and high-temperature SSC due to their excellent mechanical, chemical, thermal and optical properties [7] which can be tailored by controlling the stoichiometry ([8] and references therein). The combination of these materials into multiple configurations as semiconductor-metal tandem, metal-dielectric composite (cermet) in single, gradient or multilayer structures can achieve outstanding performance [2–4,9–19]. The material selection, the individual layer thickness and the stacking sequence play a vital role to determine the solar selective properties providing high absorptance (up to 98%) and low emittance (<15%). The SSC concept is generally comprised of an anti-reflective layer (AR), one or several absorber layers, and an infrared reflective (IR) layer next to the substrate. The AR top-layer help to decrease the reflectivity of the absorber layer and to stabilize the coating at high temperatures. The infrared reflective layer reduces the thermal emittance at high temperatures and acts as a thermal barrier to avoid material diffusion between the absorber material and the substrate. Current state-of-the-art uses physical vapour deposited (PVD) metallic interlayers to decrease the emittance. This works satisfactorily in vacuum but fails in air because of favoured thermal oxidation and interdiffusion of species along the substrate and the absorber coating. Recently, Ibrahim et al. [20] have reported a review about the solar selective performance of metal nitride/oxynitride based magnetron sputtered thin film coatings, which includes a table with the solar selectivity of SSC deposited on different substrates. In some cases, and in order to simplify the deposition process, metallic substrates (like stainless steel or Inconel alloys) are used directly as the IR-component although they have high intrinsic emittance (e.g. $\varepsilon_{24°C}$ = 28% - polished SS316) [21], leading to a low photothermal conversion efficiency. Table 1 summarizes some functional multilayer (oxy)nitride coatings reported in the literature for high temperature solar selective applications with information about optical properties and oxidation stability.

Based on the results obtained in the companion part 1 of this work [8], which reported the optical and structural properties of CrN_y and $Cr_{1-x}Al_xN_y$ films, we present in this paper the design and characterization of two multilayered SSC, based on these materials, for their potential use at high temperature. The coatings are prepared using high power impulse magnetron sputtering technique (HiPIMS), a relative novel PVD technology where higher plasma densities and ionization degree can be achieved [22,23]. These particular features allow the preparation of denser coatings, free of droplets with incomparable adhesion, which results in higher thermal and structural stability.

2. Experimental

2.1. Coating preparation and annealing treatment

Two different SSC multilayered systems (stack #1 and stack #2) were grown by HiPIMS using chromium and aluminium targets on stainless steel 316L (RMS = 61 nm), silicon (100) and quartz substrates. The constituent layers of both stacks are plotted in Fig. 1. The stoichiometries of the layers were obtained from the nominal compositions. Details of the deposition parameters of the individual CrN_y and $Cr_{1-x}Al_xN_y$ layers were given in the companion paper [8]. The aluminium layer in stack #1 was deposited with the aluminium target using HiPIMS powered at 150 W, 1000 Hz frequency and 20 μs pulse length, and with 40 sccm of Ar gas flow. The Al_2O_3 anti-reflective layer was deposited applying 300 W to the Al target at the same frequency and pulse length, with a gas mixture formed by 25 sccm of Ar and 1 sccm of O_2. The complete SSC stacks were manufactured in a single batch process.

The isothermal annealing treatments were performed in a muffle furnace in air. The samples were heated to 600, 700 and 800 °C during 2 h. A constant heating ramp of 5 °C/min was applied to reach the desired temperature.

Table 1
Summary of the optical properties and thermal stability of state of the art high temperature SSC candidate stacks. (SS = stainless steel).

SSC stack	Substrate	Ref.	α (%)	$\varepsilon_{25\,°C}$ (%)	s	Thermal stability (max. T/ambient/ time)
TiAlN/TiAlON/ Si_3N_4	Cu	[9]	95	7	13.5	600 °C/air/2 h
TiAlN/AlON	Cu	[10]	94	5	18.9	600 °C/air/2 h
	SS[a]		93	19	4.9	800 °C/air/2 h
TiAlSiN/ TiAlSiON/ SiO_2	Cu	[11]	95	11	8.6	400 °C/air/ 2500 h
TiAlCrN/ TiAlN/AlSiN	Cu	[12]	91	7	13	
	SS304		88	10	8.8	500 °C/air/4 h
TiN/AlTi(O)N/ AlTiO	Inconel HAYNES 230	[13, 14]	91	14	6.5	650 °C/air/12 h Cycles 300–600 °C/air/ 700 h
$MoSi_2$–Si_3N_4/ Si_3N_4/Al_2O_3	Inconel 625	[15]	92	13	7.1	600 °C/air/500 h
W/WSiAlN$_x$/ WSiAlO$_y$N$_x$/ SiAlO$_x$	SS304	[16]	96	11	8.7	450 °C/air/400 h
W/CrAlSiN$_x$/ CrAlSiO$_y$N$_x$/ SiAlO$_x$	SS304	[17]	95	10	9.5	450 °C/air/650 h
W/WAlSiN/ SiON/SiO_2	SS304	[18]	96	10	9.6	600 °C/ vacuum/200 h
Cr/AlCrN/ AlCrNO/ AlCrO	SS	[19]	94	10	9.6	500 °C/air/ 1000 h

[a] SS: stainless steel.

2.2. Microstructural characterization

The X-ray diffraction (XRD) patterns of the SSC deposited on 316L steel (as prepared and after annealing treatment) were obtained in a X'Pert Pro PANALYTICAL diffractometer at grazing incidence (1°) using Cu K_α radiation.

The morphology and thickness of the as-prepared stacks deposited on silicon substrates were observed by scanning electron microscopy (SEM). Cross-section views (X-SEM) were obtained cleaving the coatings. A high-resolution field emission gun (FEG) microscope, HITACHI-S4800, equipped with an energy-dispersive X-ray (EDX) detector (Bruker, XFlash-4010) was employed. Cross-sections of the as-prepared and heated SSC deposited on silicon substrates were done for the transmission electron microscopy (X-TEM) characterization, following the conventional procedure of mechanical polishing followed by argon ion milling to electron transparency. Microstructural and chemical information was then obtained using a TALOS F200S microscope from FEI company, working at 200 kV with 0.25 nm resolution, with a Super-X: 2SDD EDX and high-angle annular dark field (HAADF)-STEM detectors.

Raman spectra (200-2000 cm^{-1}) of as-prepared and heated SSCs were measured using LabRAM Horiba Jobin Yvon spectrometer equipped with a CCD detector and a diode-pumped solid state laser (532 nm) at 5 mW. All of the samples were analysed during 100 s of exposure time and with an aperture hole of 100 μm.

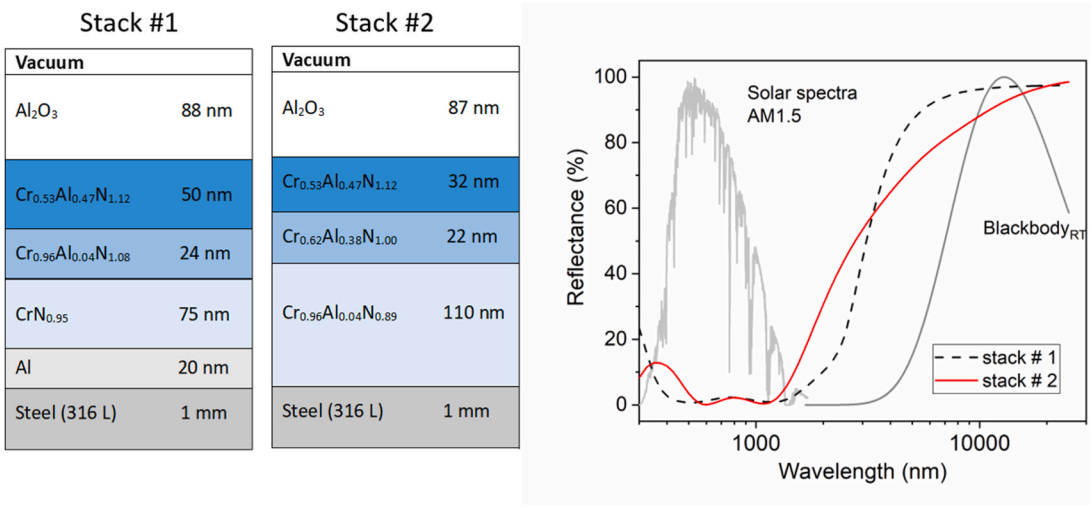

Fig. 1. (left) Schematic diagrams of the designed SSC (stack #1 and stack #2). The stoichiometries of the layers was obtained from the nominal composition. (right) Simulated reflectance spectra of the two configurations obtained by CODE software. The normalized direct + circumsolar AM 1.5 spectrum and the blackbody emission at RT are also plotted to show the selective behaviour of the coatings.

2.3. Optical characterization

The optical spectra reflectance was measured in the UV–Vis to mid-IR range (0.25–25 μm) using two different spectrophotometers: i) an UV–Vis–NIR Cary 5000 spectrometer equipped with an integrating sphere that measures in the 0.25–2.5 μm range; ii) a Fourier transform infrared (FTIR) Bruker Vertex 70 spectrometer equipped with a DLaTGS detector and KBr beam splitter that measures from 2.5 to 25 μm (400–4000 cm^{-1}), with a resolution of 0.4 cm^{-1}. A specular "W-type" accessory was employed for the FTIR reflectance measurements using a gold-coated glass as reference.

The solar absorptance α and thermal emittance ε were calculated according to the spectral reflectance by the following equations [24,25]:

$$\alpha = \frac{\int_{0.3\mu m}^{2.5\mu m}[1 - R(\lambda)]G(\lambda)d\lambda}{\int_{0.3\mu m}^{2.5\mu m} G(\lambda)d\lambda} \quad (1)$$

$$\varepsilon(T) = \frac{\int_{1\mu m}^{25\mu m}[1 - R(\lambda, T)]B(\lambda, T)d\lambda}{\int_{1\mu m}^{25\mu m} G(\lambda, T)d\lambda} \quad (2)$$

where $R(\lambda)$ is the spectral reflectance of the sample, $G(\lambda)$ is the solar radiation power at AM1.5, and $B(\lambda, T)$ is the spectral black body emissive power at temperature T [26]. Note that emittance integration range covers from $\lambda = 1$ μm to $\lambda = 25$ μm based on European standard EN-673:2011 [25].

The performance criterion of a solar selective surface, is, generally, evaluated by the ratio of solar absorptance to the thermal emittance $s = \alpha/\varepsilon$, where "s" is known as the solar selectivity [19]. Two additional parameters will be used to compare the performance of the SSC:

1) The solar-to-mechanical energy conversion efficiency, or solar performance (η), estimated according to the expression [4]:

$$\eta(T) = \eta_{optical} \cdot \eta_{Carnot} = \left(\alpha - \frac{\varepsilon(T)\cdot\sigma(T^4 - T_0^4)}{C\cdot I}\right)\left(1 - \frac{T_0}{T}\right) \quad (3)$$

where C is the solar concentration ratio, I is the incident solar flux density [W/m^2], σ is the Stefan-Boltzmann constant, T and T_0 are the receiver and ambient temperature [K], respectively. The following parameters were considered for the calculation: $C = 100$ and 1000 [27], $I = 1000$ W/m^2, $T = 600$ °C (873 K), 700 °C (973 K) and 800 °C (1073 K), $T_0 = 298$ K.

2) The performance criterion (PC), calculated from the obtained optical properties using the equation [28]:

$$PC = -\Delta\alpha + 0.5\Delta\varepsilon \quad (4)$$

where $\Delta\alpha = \alpha$ (aged) $- \alpha$ (unaged), and $\Delta\varepsilon = \varepsilon$ (aged) $- \varepsilon$ (unaged). Acceptable PC should be lower than 0.05 (5%), otherwise the coating is identified as failed [28].

3. Results and discussion

3.1. Design of optimized multilayer solar selective coatings

$Cr_{1-x}(Al)_xN_y$ multilayer based-SSC with different constituents were designed using CODE software [29]. In Fig. 1, the two SSC showing the best optical performance in terms of α and ε simulated values are presented. The layer structure of these solar absorbers deposited on 316L steel substrates (from bottom to top) is as follows: stack #1 uses an Al layer as IR reflector, and a bilayer of $CrN_{0.95}$ and $Cr_{0.96}Al_{0.04}N_{1.08}$ films acting as main solar absorbers. Meanwhile, stack #2 applies a $Cr_{0.96}Al_{0.04}N_{0.89}$ layer both as IR reflector and solar absorber, and $Cr_{0.62}Al_{0.38}N_{1.00}$ film as a semi-absorber layer. In both stacks these layers are followed by a $Cr_{0.53}Al_{0.47}N_{1.12}$ film to decrease the refractive index until reaching the anti-reflective Al_2O_3 top-layer. The multilayered architecture, the high Al content of the top $Cr_{1-x}Al_xN_y$ layer ($Cr_{0.53}Al_{0.47}N_{1.12}$) and the protection given by the surface Al_2O_3 layers, are expected to convey a high temperature oxidation resistance to these SSC [30,31].

The optical properties of the solar absorbers mainly depend on the optical constants ($n(\lambda)$ and $k(\lambda)$) and thicknesses of the individual layers. Once $n(\lambda)$ and $k(\lambda)$ have been obtained (see below), the commercial CODE software optimized the thickness of each layer in order to maximize the solar absorptance and minimize the thermal emittance.

The $n(\lambda)$ and $k(\lambda)$ values of CrN_y, $Cr_{1-x}Al_xN_y$ (see part 1 [8]) and Al_2O_3 single layers were extracted from the transmittance and reflectance measurements using appropriated dielectric function models for the spectral range (0.25–2.5 μm). The infrared spectral range, which is important for the emittance, is dominated by the highly reflective Al layer (stack #1) and $Cr_{0.96}Al_{0.04}N_{0.89}$ (stack #2). The substrate, 316L steel, is also considered as a IR layer [32]. The optical constants of these IR layers were derived from the fitting of its reflectance spectra for the whole spectral range (from 0.3 to 25 μm) using the models provided in Refs. [32].

The optimized reflectance spectra of the two configurations (stacks #1 and #2) are shown in Fig. 1. The AM1.5 direct (+circumsolar) spectrum [26] and the blackbody emission at room temperature (RT) are also represented to show the excellent solar selectivity (high solar absorptance and a low thermal emittance) of both stacks ($\alpha > 95\%$, $\varepsilon_{25\,^{\circ}C} < 8\%$, see Table 2). These simulated configurations were experimentally deposited. The details on the stack morphologies and composition, optical performance and thermal stability are described in sections 3.2, 3.3 and 3.4, respectively.

3.2. Stack morphologies and composition depth profiles

The cross-section morphologies of the as-deposited stacks were analysed by SEM and TEM, and the corresponding representative images are shown in Fig. 2(left) and 2(right), respectively. The stack thicknesses are in good agreement with the nominal values (cf. Fig. 1). Both stacks display a cauliflower surface morphology because of the typical columnar growth. The different layers constituting the stacks can be clearly distinguished in the TEM images. In stack #1, the first aluminium layer is not homogenous and grows forming small islands. The formation of hillocks on Al thin films is a well-known phenomenon determined by the interface atomic diffusion and the binding forces to the substrate [33]. A conformal growth of the subsequent layers is observed on top of these particular features, leading to an open porosity at the column boundaries. In addition, the formation of voids is clearly visible at the interface between the $Cr_{0.53}Al_{0.47}N_{1.12}$ and the topmost oxide layer (Al_2O_3). On the other hand, the stack #2 presents a denser structure and a superficial morphology ended by smaller grains in agreement with the formation of thinner columns.

In Figs. 3 and 4, HAADF-STEM images (a), EDX elemental maps (b) and elemental composition line profiles (c) obtained along the stacks #1 and #2 showing the different layers composing the stacks are presented. In stack #1, the chemical composition of the Cr(Al)N deposited layers differs a little from nominal values. The interfaces between the nitride layers are not clearly defined due to metallic interdiffusion processes. The changes in Al and Cr concentrations occur gradually affecting the definition of the thinner layers. This is particularly the case of the $Cr_{0.96}Al_{0.04}N_{1.08}$ layer, which exhibits a gradient metal composition along its entire thickness. In addition, a lower N/Cr ratio than the nominal 0.95 is observed in the absorber $CrN_{0.95}$ film. In stack #2, although sharper interfaces are observed, a small gradual Al-decrease layer seems to be formed instead of a sole $Cr_{0.62}Al_{0.38}N_{1.00}$ layer. A thin region, with N/Cr ratio lower than expected is also observed in the interface with the substrate (see the arrow in Fig. 4c). It is worth noting that, in both stacks, the oxygen content inside the internal Cr(Al)N layers is higher (~10 at.%) than the one determined by electron probe microanalysis in the companion paper (<5 at.%) [8]. This can be due to a surface oxidation of the very thin specimen prepared for TEM observation and can, therefore, alter the measured element ratios.

3.3. Optical characterization

Fig. 5 depicts the simulated and experimental reflectance spectra of the two designed stacks in the full spectral range. Both coatings display the typical dark blue colour of SSC (see the photographs of Fig. 5). These spectra present some differences, mainly in the IR range, when compared with the CODE simulated ones. These differences are clearly reflected in Table 2, where the corresponding experimental solar absorptance, thermal emittance (at 25 °C) and solar selectivity are summarized. The experimental α values are in quite good agreement with the obtained by CODE simulation, while the experimental ε values (14–15%) are higher than the simulated ones (4–8%). The discrepancies can be attributed to the aforementioned changes observed in the composition and thickness of the formed layers. In the case of stack #1, the growth of a non-homogeneous Al film, with areas of negligible thickness, is likely responsible of the increase in the emittance. A very good fitting of the experimental spectra of this stack (cf. Fig. 5) has been obtained using CODE software [29] considering the following facts: 1) the formation of a thinner Al layer (4 nm) than the nominal one to take into account the formation of disconnected aluminium islands; 2) the growth of a $CrN_{0.67}$ layer with a lower N/Cr ratio than the nominal $CrN_{0.95}$; and 3) using two additional $Cr_xAl_{1-x}N$ layers ($Cr_{0.62}Al_{0.38}N_{1.00}$ and $Cr_{0.77}Al_{0.23}N_{1.13}$) as an approximation to the observed gradual Al decrease. The optical constants of the used layers ($CrN_{0.67}$, $Cr_{0.62}Al_{0.38}N_{1.00}$ and $Cr_{0.77}Al_{0.23}N_{1.13}$) were obtained in the companion paper [8]. Values of $\alpha = 96.0\%$ and $\varepsilon = 13.0\ \%$ are obtained with this

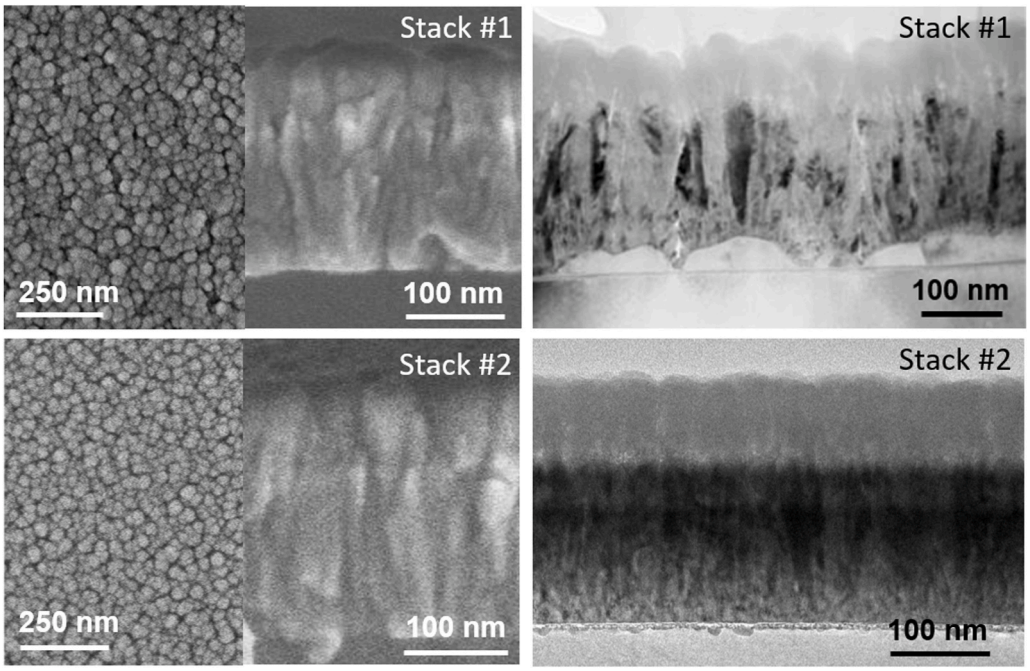

Fig. 2. (left) SEM cross-section and top view micrographs of stack #1 (top) and stack #2 (bottom). (right) cross-section TEM images of stack #1 (top) and stack #2 (bottom).

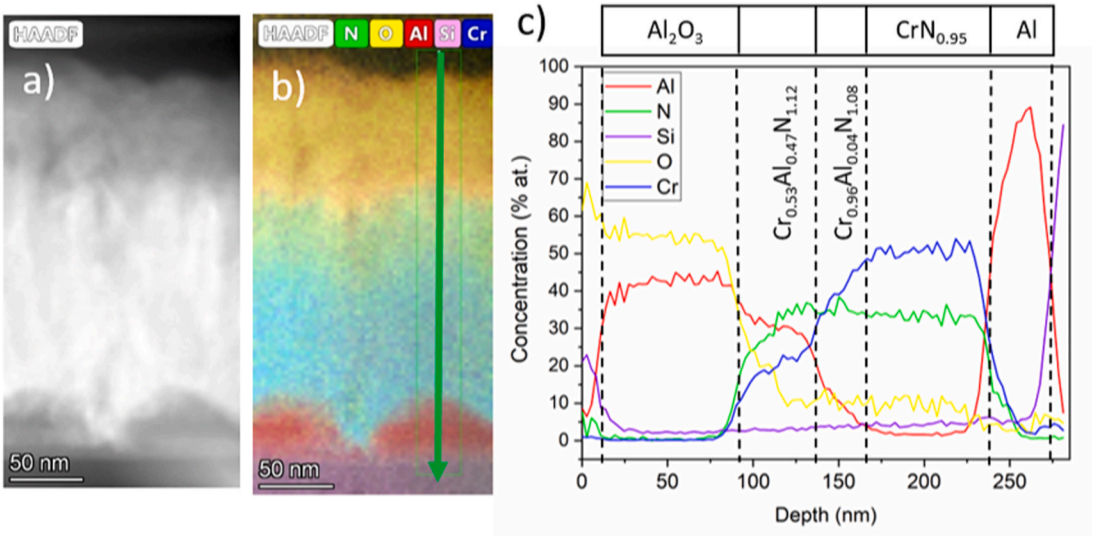

Fig. 3. (a) HAADF-STEM images (b) EDX elemental map and (c) elemental composition line profile obtained along a cross-section of the stack #1. The guidelines mark the corresponding layer divisions as depicted in Fig. 1.

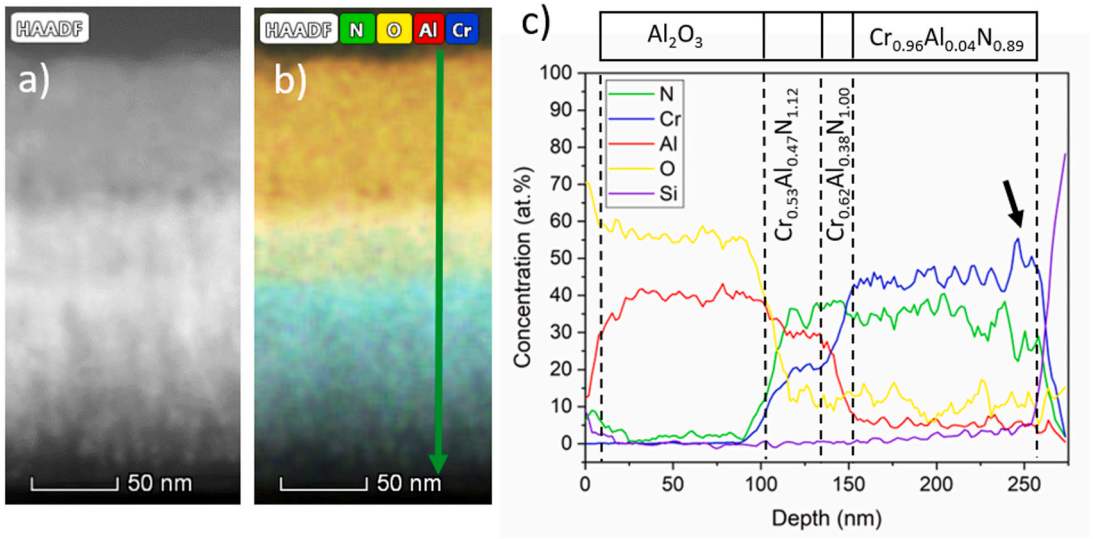

Fig. 4. (a) HAADF-STEM images (b) EDX elemental map and (c) elemental composition line profile obtained along a cross-section of the stack #2. The guidelines mark the corresponding layer divisions as depicted in Fig. 1.

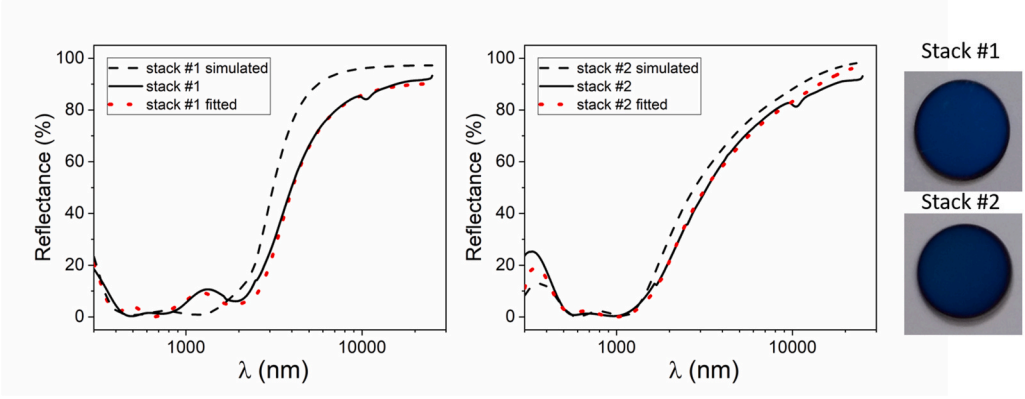

Fig. 5. Experimental, simulated and fitted reflectance spectra of stack #1 and stack #2. (Right) Optical photographs of both stacks.

Table 2
Solar absorptance, thermal emittance (at 25 °C) and solar selectivity, calculated from the simulated, experimental and fitted reflectance spectra for stack #1 and stack #2.

		α (%)	$\varepsilon_{25\ °C}$ (%)	s
Stack #1	Simulated	97.3	3.7	26.3
	Experimental	96 ± 1	14 ± 1	6.9
	Fitted	96.0	13.0	7.4
Stack #2	Simulated	95.4	7.7	12.4
	Experimental	96 ± 1	15 ± 1	6.4
	Fitted	95.5	12.5	7.6

approximation in closer agreement with the experimental ones. In the case of stack #2, a very good fitting was also obtained considering the formation of a thin layer (25 nm) of $CrN_{0.67}$ prior to the $Cr_{0.96}Al_{0.04}N_{0.89}$. Values of $\alpha = 95.5\%$ and $\varepsilon = 12.5\%$ are obtained with this approximation, again in closer agreement with the experimental ones.

The calculated values of solar absorptance and thermal emittance (at 25 °C) for both stacks (Table 2) are similar despite of the difference observed in their reflectance spectra. However, the thermal emittances at high operating temperature (600 °C) (see Table 3) show clear differences between the two as-deposited stacks. In particular, lower values are obtained for stack #2.

The solar performance (η) of both stacks was calculated using Eq. (3) for two concentration factors (C = 100 and 1000) that cover typical values for central receiver tower plants in operation or under construction [26]. The values were compared with Pyromark performance at target working temperatures T = 600, 700 and 800 °C. Data of Pyromark absorptance ($\alpha_{Pyro} = 96\%$) and emittance ($\varepsilon_{Pyro}\ \varepsilon_{25\ °C} = 86\%$) was taken from literature [34,35]. For C = 100, there is a significant improvement in the performance of the stacks as compared to Pyromark (see Fig. 6a). At a target working temperature of 700 °C, the improvement in performance of the deposited stacks is substantial, with a ≈15% points higher than the Pyromark efficiency at such temperature. Even more, at T = 800 °C the performance of the selective stacks is about double the one of the absorber paint. In other words, the selective stacks require lower concentration factors than Pyromark to achieve the same efficiencies. For higher C values (C = 1000), the performance of the stacks is comparable to Pyromark (≈1–2% better) (see Fig. 6b). This is in line with the evidence that, at very high concentration factors, the predominant parameter is the absorptance of the receiver rather than its selectivity.

In summary, the RT optical performance of the current SSC stacks deposited on steel (α > 95%, ε < 15%, $\eta \geq \eta_{Pyromark}$ for C = 100 and 1000) places them among the best candidates for air-stable SSC working at high temperature (cf. Table 1 and [19]). In the following section, the thermal stability of the deposited stacks is reported.

3.4. Thermal stability of the stacks

3.4.1. Optical characterization of the annealed samples

The SSC were heated up to 600, 700 and 800 °C during 2 h in air to study their thermal stability and optical behaviour. In Fig. 7, the reflectance spectra obtained at each temperature are plotted for both stacks. The changes observed, mainly above 600 °C, will be analysed below, when the structural characterization will be presented. The values of α, $\varepsilon_{25\ °C}$ are shown in Table 3, and its evolution with the temperature together with the performance criterion of both stacks are plotted in Fig. 8a, (b) and 8(c), respectively. For stack #1, a decrease of α and ε is observed from RT to 600 °C, and then stabilized at 700 °C. For stack #2, a continuous decrease of α and $\varepsilon_{25\ °C}$ is observed up to 700 °C. In spite of these changes, both stacks fulfilled the defined PC criterion (see Eq. (4)) after the thermal treatment up to 700 °C (see Fig. 8c). In particular for stack #2, the decrease of α with the thermal treatment is levelised with a significant low emittance at 700 °C. This is a very remarkable result considering that the emittance of the substrate (316L) increases considerably with the temperature (i.e. $\varepsilon_{316L} \simeq 35\%$ at 500 °C [21]), and will be further explained in the post heating structural characterization. The thermal emittances at 600 °C, obtained for the annealed stacks, have also been added in Table 3. Clear differences between the two stacks are observed, and, as in the as-deposited stacks, lower values are obtained for stack #2. Finally, a significant degradation of the optical performance is observed at 800 °C for both stacks (α decreases below 88% and ε rises up to 22%) with a PC clearly above the limit of 5%. The original dark blue colour of the samples is conserved until the treatment at 700 °C, turning into yellow-brownish appearance at 800 °C indicative of the beginning of the oxidation.

This good thermal behaviour at high temperature has a clear impact in the solar-to-mechanical energy conversion efficiency (η) of the annealed stacks. Fig. 9 shows the evolution of η of the annealed samples (600, 700 and 800 °C) for two target working temperature operations (600 and 700 °C) and a concentration factor C = 100. It can be observed how all annealed stacks outperformed Pyromark in these scenarios. Annealed samples at 600 °C present an efficiency similar to the as-deposited stacks, that is, at least 10% points higher that Pyromark efficiencies for the same working temperatures. The samples annealed at 700 °C boosted their efficiencies reaching outstanding values of 55% for such a relative low concentration factor. This value is 20% points higher than Pyromark efficiency at this working temperature. As expected, samples annealed at 800 °C present a clear decrease in the solar efficiency due to the degradation of the optical performance associated to an oxidation process. The efficiency increase in respect to Pyromark is even larger (≈30%) at a target working temperature of 800 °C but as the stacks were found to be degraded after 2 h of annealing at such temperature, the results are not shown here (see Fig. 1 in the supplementary material).

For higher C values (C = 1000), the performance of both stacks annealed at 600 °C and that of stack #1 at 700 °C is just comparable to Pyromark (see Fig. 2 in supplementary material). However, the strong decrease in α observed for stack #2 annealed at 700 °C and both stacks at 800 °C, cannot be compensated by the parallel decrease in emittance. Hence, the solar efficiencies of such samples are lower than the corresponding one of Pyromark both at those target temperatures (600 °C and 700 °C). All these results are presented in the supplementary material.

Taking into account the above reported stability (at least in the short term) of the stacks annealed up to 700 °C, these efficiency results foresee an optimal performance of the multilayers at a target operating temperature T ≤ 700 °C, that is 150 °C higher than the current technology.

Table 3
Solar absorptance and thermal emittance (at 25 and 600 °C) obtained for the annealed stacks at 600, 700 and 800 °C during 2 h. The values for as-prepared stacks are added for comparison. The error in the experimental values were estimated to be of ±1% for α and ε.

	As deposited			600 °C			700 °C			800 °C		
	α	ε_{25}	ε_{600}	α	ε_{25}	ε_{600}	α	ε_{25}	ε_{600}	α	ε_{25}	ε_{600}
	(%)			(%)			(%)			(%)		
Stack #1	96	14	44	94	12	44	94	12	25	87	22	60
Stack #2	96	15	38	93	13	38	88	6	16	86	22	39

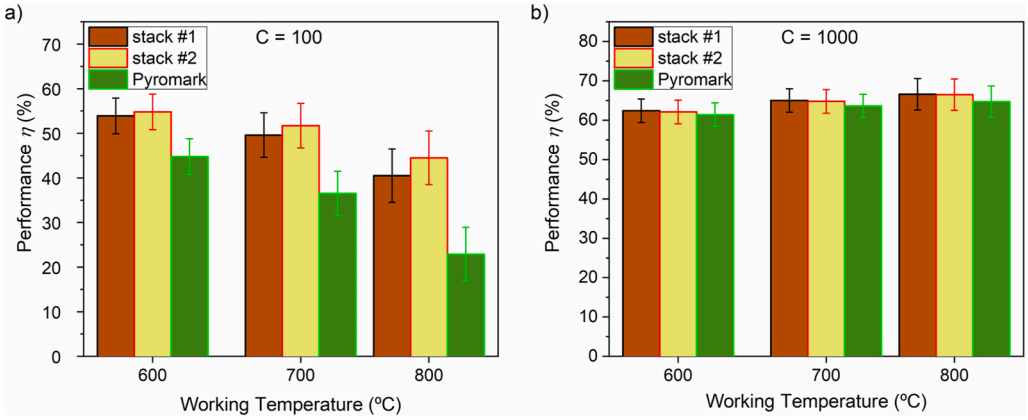

Fig. 6. Calculated solar performances η of both as-deposited stacks at target working temperatures of 600, 700 and 800 °C for concentration factors (a) C = 100 and (b) C = 1000. Results obtained for Pyromark performances are also presented for comparison.

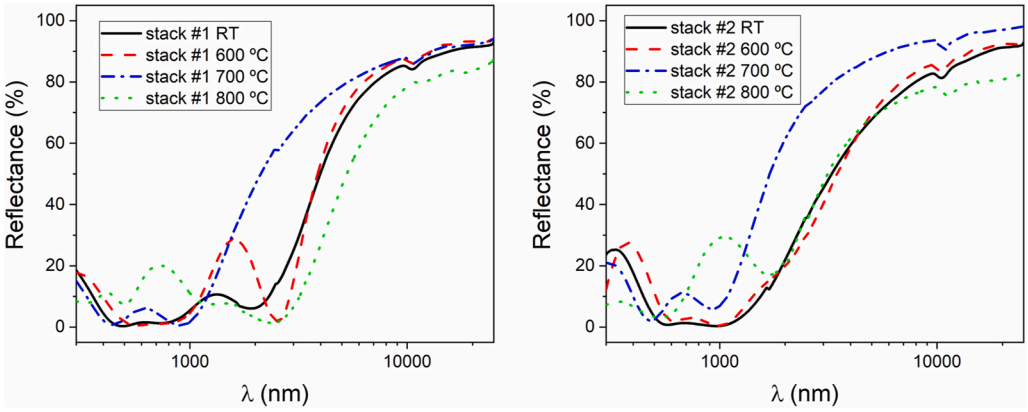

Fig. 7. Reflectance spectra of the as-deposited (RT) and annealed (600, 700 and 800 °C) stacks during 2 h in air.

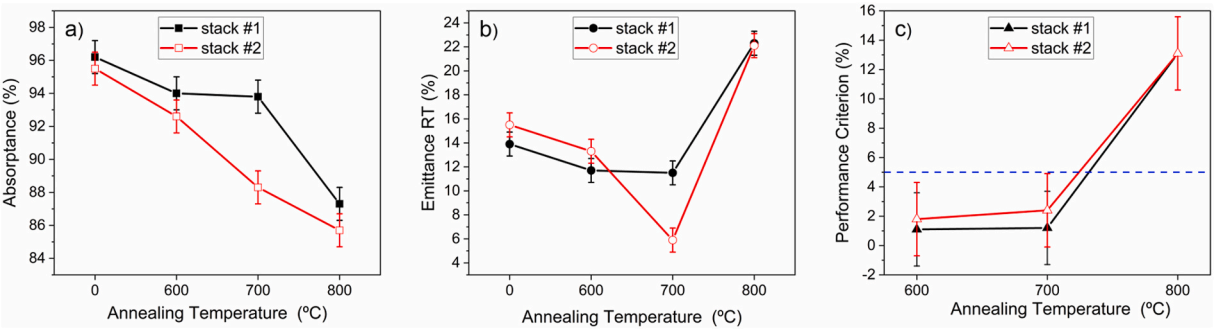

Fig. 8. Evolution of the (a) solar absorptance α, (b) thermal emittance ε, and (c) performance criterion measured after the single-stage thermal tests performed at 600, 700 and 800 °C for stack #1 (solid symbols) and stack #2 (open symbols). In (c) a horizontal dotted line is plotted to mark the threshold of PC = 5%.

3.4.2. *Microstructural characterization of the annealed samples*

In order to understand the changes of the optical performance with the annealing temperatures, an investigation of the induced microstructural and compositional changes was conducted using Raman spectroscopy, XRD, SEM and TEM measurements. Fig. 10 shows the Raman spectra for the stack #1 and #2, as-prepared and after 2 h of thermal treatment in air at 600, 700 and 800 °C. No transformation is observed for both stacks either at 600 °C or at 700 °C that could explain the small variations observed in α and ε values. The weak and broad bands centred at 250 and 700 cm^{-1} are attributed to acoustic and optic phonons vibrations in defective non-stoichiometric Cr(Al)N, respectively, as allowed first-order Raman active phonon vibrations are forbidden in perfect *fcc*-lattice structures. Increasing the temperature, the acoustic modes remain almost in the same position but a gradual shift is observed in the phonon band towards higher values. This shift towards higher frequencies can be correlated to an increasing aluminium content in the outer layers and/or nitrogen vacancies induced during heating as observed previously [36,37]. At 800 °C, however, a wide band composed of two sharp peaks at 580 and 695 cm^{-1} is observed for stack #1. These Raman features can be assigned to a mixture of chromium oxides (Cr_2O_3, $Al_xCr_{2-x}O_3$, CrO_2 [38,39], indicating the oxidation onset of the stack #1. These peaks are not clearly formed in stack #2 at the same temperature, what demonstrates a higher oxidation resistance.

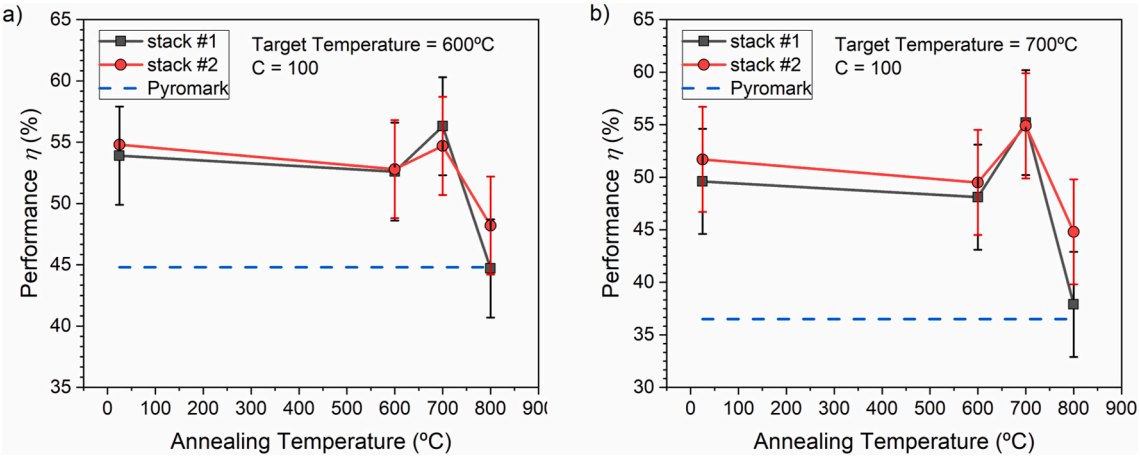

Fig. 9. Evolution of the solar performances η of the annealed stacks calculated at two target working temperatures of (a) T = 600 °C and (b) T = 700 °C, and a concentration factor C = 100.

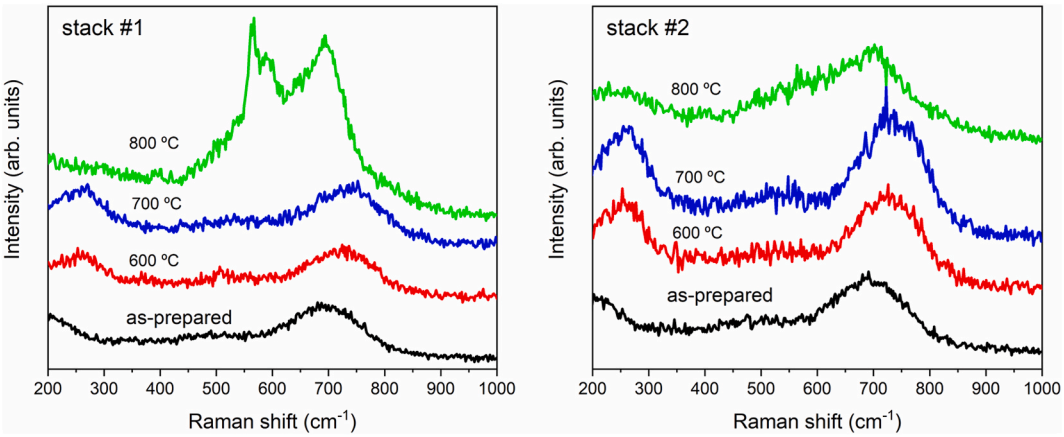

Fig. 10. Raman spectra of the as-prepared and annealed stacks.

The XRD spectra of the as-prepared stacks (on quartz) and after annealing at 600, 700 and 800 °C (on SS 316L) during 2 h are depicted in Fig. 11. The diffractograms of the initial stack #1 is congruent with a *fcc*-CrN carlsbergite structure. The diffraction peaks of the steel substrate can be observed in the heated coatings for both stacks due to their limited thickness (~250 nm) despite using a grazing angle for X-ray incidence. It is worth mentioning that the most intense peak of the substrate at 43.6° matches with the (200) of the *fcc*-CrN carlsbergite structure although the chromium nitrides peaks are generally shifted towards higher 2θ angles. The right-shift observed in the CrN peaks is due to the Al incorporation in the last $Cr_{1-x}Al_xN_y$ layer ($Cr_{0.53}Al_{0.47}N_{1.12}$) and the existence of N vacancies in the $CrN_{0.95}$ layer, leading to a lattice contraction as demonstrated previously in Part 1 [8]. The peak positions of these two individual layers, measured in the companion paper, are also depicted. The broadening of the peaks is also a consequence of the reduction of crystalline domains caused by the presence of lattice defects and non-stoichiometric phases. Both effects are significantly reduced after the thermal treatment at 600 °C although the formation of new phases do not appear clearly until 700 °C. At this point, some new peaks assigned to the hexagonal Cr_2N phase are produced by the thermal decomposition of more unstable $CrN_{0.95}$ and $Cr_{0.96}Al_{0.04}N_{0.89}$ layers [31,40,41], and in less extent of $Cr_xAl_{1-x}N_y$ due to the higher stability of the Al-containing layers [31,39]. At 800 °C, the main peaks are originated by chromium and iron oxides (Cr_2O_3, Fe_3O_4) and the steel substrate. The presence of a new iron phase (Fe-3) and iron oxides is the result of the iron out-diffusion from the substrate and the inwards oxygen penetration toward the substrate. This result might explain that the decay of the optical properties at this temperature is due to the degradation of the substrate material rather than of the multilayer coating.

The as-deposited stack #2 also exhibits the characteristic peaks of *fcc*-CrN carlsbergite structure with a right-shift and split into two components, corresponding to the $Cr_{0.53}Al_{0.47}N_{1.12}$ and $Cr_{0.96}Al_{0.04}N_{0.89}$ layers, respectively (see Part 1 [8]). The formation of Cr_2N is already relevant in this case at 600 °C as compared to stack #1. However, the peaks due to the $Cr_{1-x}Al_xN_y$ phase and the peaks associated to oxidation and interdiffusion processes are less intense. Similar to stack #1, a Fe-3 peak is also revealed at 800 °C at 44° related to iron diffusion from the substrate during annealing. This migration through the film alters both stack configurations, degrading their optical performance. Consequently, further studies with alternative substrates suitable for high temperatures should be carried out to determine accurately the thermal resistance of the coatings.

The stacks deposited on silicon and heated at 700 °C in air during 2 h were also analysed by X-SEM and X-TEM. Fig. 12 demonstrates that no big changes are appreciated in the microstructure by SEM cross-sectional views (cf. Fig. 2 left). The stack #1 exhibits bigger column sizes and intercolumnar porosity than in the as-deposited state, while the stack #2 retains the original denser morphology.

A representative HAADF-STEM image of the heated stack #1 at 700 °C is presented in Fig. 13 together to the associated X-EDS elemental map and line profile composition. The most important aspect observed in the line profile is that the oxygen penetrated into the $Cr_{1-x}Al_xN_y$ and

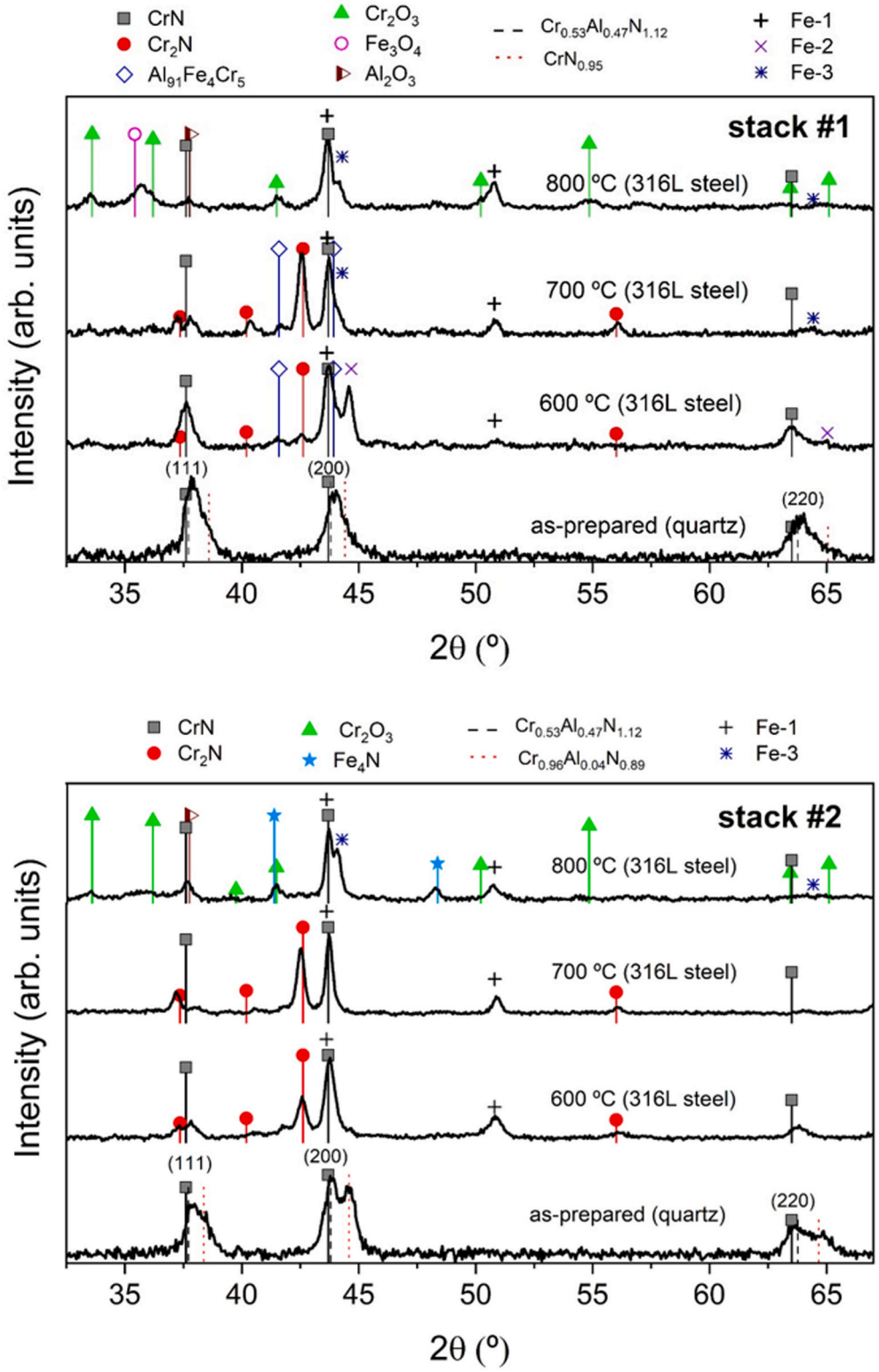

Fig. 11. XRD diffractograms of as-prepared and annealed stacks measured in glancing angle configuration. JCPDS cards numbers: CrN (PDF #76–2494); Cr_2N (PDF #35–803); $Al_{91}Fe_4Cr_5$ (PDF #45–1018); Cr_2O_3 (PDF #38–1479); Fe_3O_4 (PDF #19–0629); Al_2O_3 (PDF #1-77-2135); Fe_4N (PDF #1–1219; Fe-1 (PDF #96-900-8470); Fe-2 (PDF #96-900-6658); Fe-3 (PDF #96-901-3478).

$CrN_{0.95}$ layers, reaching the substrate and oxidizing the aluminum layer. Despite of the progress of the oxidation, a very thin Al metallic layer seems to be still present in the interface (see the arrows in the X-EDS map and in the Al profile). Other outstanding observed aspects are the diffusion (both outwards and inwards) of chromium, aluminium (in lesser extent), silicon and the out-diffusion of nitrogen forming an $(Al, Cr)_x(N,O)_y$ intermediate region between the Al_2O_3 and $Cr_{1-x}Al_xN_y$ layers.

In the case of stack #2, the oxygen only penetrated slightly into the first $Cr_{1-x}Al_xN_y$ layer (cf. Fig. 14) and no silicon diffusion is observed along the coating. These results are demonstrating the more protective

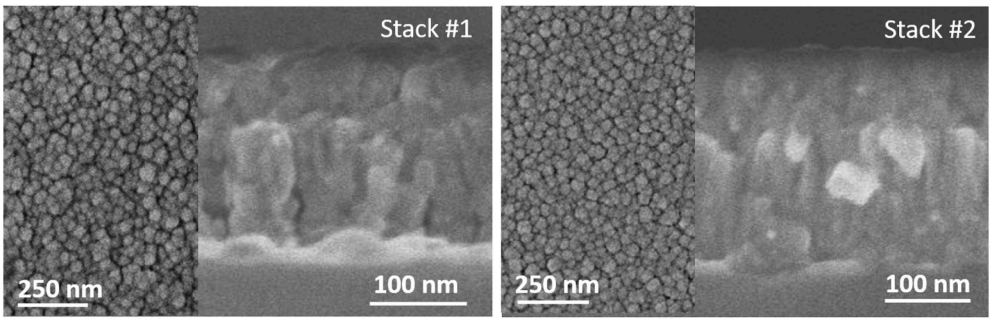

Fig. 12. SEM cross-section and top view micrographs of the stacks heated at 700 °C during 2 h.

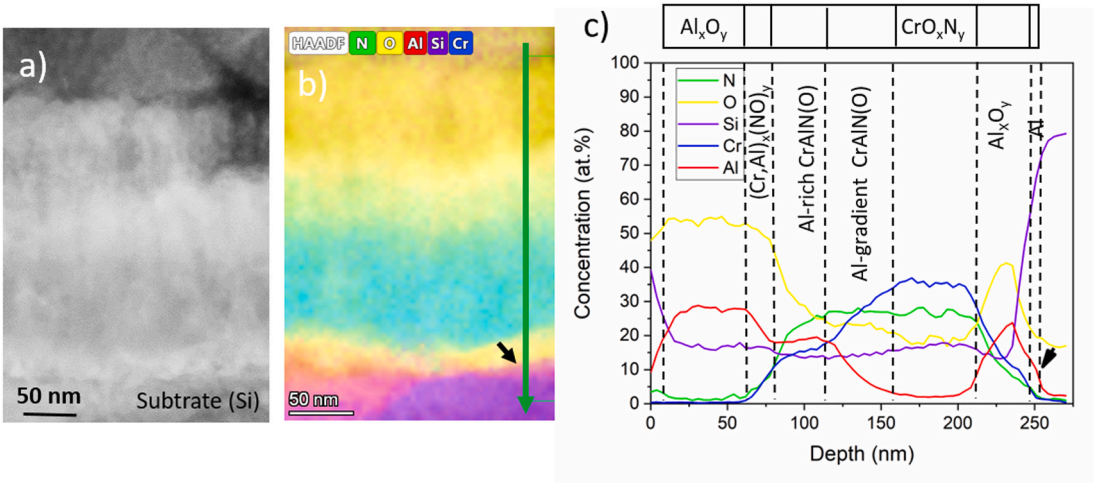

Fig. 13. (a) HAADF-STEM images, (b) EDX elemental map and (c) elemental composition line profile obtained along the stack #1 after heating at 700 °C during 2 h. The guidelines mark the layers after the thermal treatment.

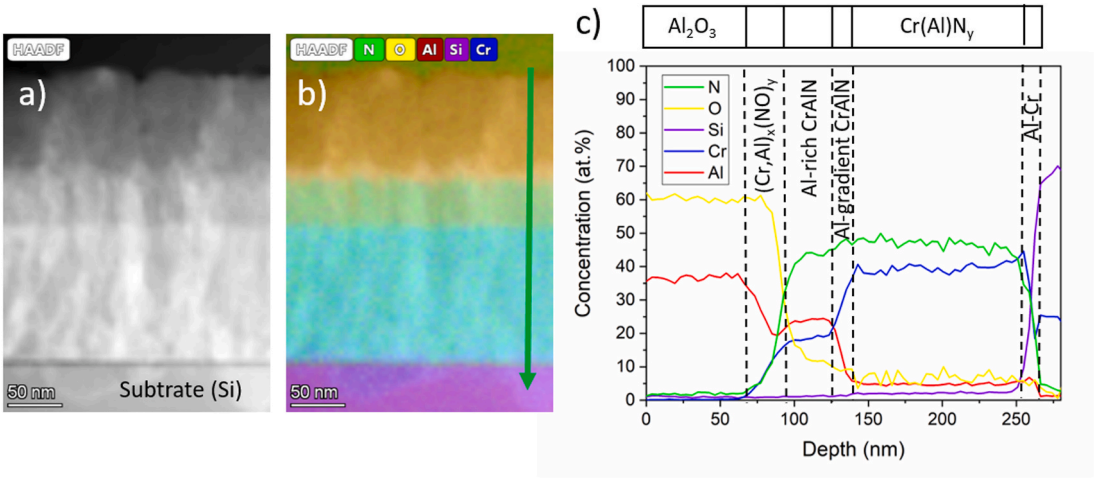

Fig. 14. (a) HAADF-STEM images, (b) EDX elemental map and (c) elemental composition line profile obtained along the stack #2 after heating at 700 °C during 2 h. The guidelines mark the layers after the thermal treatment.

character and oxidation resistance of this stack preventing the oxygen penetration and the substrate elements out-diffusion. The element diffusions (Cr, Al and N) and the formation of the $(Al,Cr)_x(N,O)_y$ layer are also observed in this stack #2. A new thin Al–Cr layer is, therefore, detected in the interface with the substrate. The higher porosity and the presence of the Al inner layer (which acts as an oxygen trap) would explain the lower oxidation resistance of stack #1.

In both stacks, a decrease in the nitrogen content is not detected as could be expected from the formation of hexagonal Cr_2N observed by XRD. The different type of substrate (silicon here instead of the 316L stainless steel used in XRD) could account for the different behaviour. The 316L steel substrate favours the decomposition of CrN to Cr_2N versus a more inert substrate as a silicon wafer [30]. This result further confirms the influence of the substrate composition on the thermal stability of the layers as previously reported [30]. Nevertheless, very valuable and unique information has been obtained from the STEM-EDX

analysis of the annealed stacks deposited on silicon that will help to understand the observed optical behaviour.

Hence, for stack #1, the decrease observed in the absorptance at 600 °C and 700 °C can be due to the formation of a $(Al,Cr)_x(N,O)_y$ region below the Al_2O_3 layer, and the partial oxidation of the inner Cr(Al)N layers. Furthermore, the lower emittance values at these temperatures can be explained by the transformation of $CrN_{0.95}$ to Cr_2N (more metallic) and the remaining Al metallic layer (3 nm). Based on these results, we have fitted the experimental reflectance spectra of the annealed stack #1 using previous studied layers [8] with approximate chemical composition (see Fig. 3a of supplementary material).

In the case of stack #2, the observed decrease in the absorptance is likely to be explained as well in terms of the formation of a thicker $(Al,Cr)_x(N,O)_y$ layer than in the stack #1. The decrease of the thickness of $Cr_xAl_{1-x}N_y$ inner layers (by the partial oxidation and Al diffusion) would explain the decrease of the absorptance at 700 °C. In parallel, the formation of Cr_2N, with more metallic character and more IR-reflective than $Cr_{0.96}Al_{0.04}N_{1.08}$ [8], and the formation of a Al–Cr metallic layer beneath the interface with the substrate would account for the remarkable decrease observed in the emittance at 700 °C (see Fig. 3b of supplementary material with the fitting obtained for the annealed stack #2).

4. Conclusions

Two SSC based on $Cr_{1-x}(Al_x)N_y$ layers were designed and prepared by DC/HiPIMS technology to be evaluated as candidates for high temperature applications. Good agreement between simulated and experimental optical performance was found for the two multilayer SSC stacks that presented high absorptance in the UV–Vis region ($\alpha > 95\%$) and low thermal emittance in the infrared range ($\varepsilon_{25\,°C} < 15\%$).

The stacks were studied after thermal treatment in air at 600, 700 and 800 °C during 2 h, and result to be stable up to 600 °C. Despite of some structural and compositional changes, above 600 °C, both stacks showed at 600 °C and 700 °C similar dark blue colour than initially and fulfilled the criterion performance (measured PC values $\leq$ 2.5%). The optical properties were found to be optimum up to 700 °C for stack #1 ($\alpha = 94\%$, $\varepsilon_{25\,°C} = 12\%$) and 600 °C for stack #2 ($\alpha = 93\%$, $\varepsilon_{25\,°C} = 13\%$). Nevertheless, the stack #2 demonstrated a higher oxidation resistance than stack #1 and could be a promising candidate for further thermal studies (longer duration and cycling). At 800 °C, the stacks underwent a structural transformation caused by the oxidation of the $Cr_x(Al)_{1-x}N_y$ layers, as evidenced by Raman and XRD results, leading to a significant degradation of the optical properties. Nevertheless, a negative influence of the steel substrate unstable at this temperature may be not discarded. The characterization by TEM techniques (EDX mapping and line profile) of the as-prepared and annealing stacks has resulted fundamental to understand their optical behavior.

The as-prepared and annealed stacks at 600 and 700 °C stacks present better solar-to-mechanical energy conversion efficiency (η) than the absorber paint commercially used (Pyromark), for a concentration factor C = 100. The efficiency results foresee an optimal performance of the multilayers at a target operating temperature T $\leq$ 700 °C, that is indeed 150 °C higher than the current technology. The current results also proved the importance of a suitable microstructural and chemical characterization of the heated stacks deposited on the substrate to be used in the foreseen application.

Future investigations must be carried out to assess the limit working temperature for both stacks during long duration and cycling experiments. The employment of alternative substrate for high temperature as Inconel is necessary to avoid the influence of diffusion processes of element substrates during heating.

CRediT authorship contribution statement

T.C. Rojas: Conceptualization, Methodology, Software, Formal analysis, Visualization, Investigation, Writing - original draft, Writing - review & editing. **A. Caro:** Software, Formal analysis, Investigation. **R. Escobar-Galindo:** Visualization, Formal analysis, Writing - review & editing, Supervision. **J.C. Sánchez-López:** Conceptualization, Methodology, Visualization, Investigation, Supervision, Writing - review & editing, Funding acquisition.

Declaration of competing interest

The authors declare that they have no known competing financial interests or personal relationships that could have appeared to influence the work reported in this paper.

Acknowledgments

European Regional Development Funds program (EU-FEDER), Spanish Ministry of Economy, Industry and Competitiveness (project no. MAT2015-65539-P), Spanish Ministry of Science and Innovation (project no. PID2019-104256RB-I00) and Junta de Andalucía (PAIDI2020 project no. P18-RT-2641) are acknowledged for financial support. The authors would like to acknowledge the technical support of M[a] Carmen Gutiérrez Lázaro with the UV–Vis measurements and Wolfgang Theiss (www.mtheiss.com), for providing the model to get the dielectric function of the IR layers in the IR energy range and for his inestimable help during the fitting of the reflectance spectra.

Appendix A. Supplementary data

Supplementary data to this article can be found online at https://doi.org/10.1016/j.solmat.2020.110812.

References

[1] Renewables 2019: global status report: a comprehensive annual overview of the state of renewable energy, REN21, http://www.ren21.net/gsr-2019/, 2019. (Accessed 15 September 2020).
[2] C. Atkinson, C.L. Sansom CL, H.J. Almond, C.P. Shaw Cp, Coatings for concentrating solar systems-A review, Renew. Sustain. Energy Rev. 45 (2015) 113–122.
[3] N. Selvakumar, H.C. Barshilia, Review of physical vapor deposited (PVD) spectrally selective coatings for mid- and high-temperature solar thermal applications, Sol. Energy Mater. Sol. Cells 98 (2012) 1–23.
[4] A. Soum-Glaude, A. Le Gal, M. Bichotte, C. Escape, L. Dubost, Optical characterization of $TiAlN_x/TiAlN_y/Al_2O_3$ tandem solar selective absorber coatings, Sol. Energy Mater. Sol. Cells 170 (2017) 254–262.
[5] A. Ambrosini, A. Boubault, C.K. Ho, L. Banh, J.R. Lewis, Influence of application parameters on stability of Pyromark® 2500 receiver coatings Cite as, AIP Conf. Proc. 2126 (2019), 030002.
[6] https://www.solec.org/solkote/concentrating-applications/. (Accessed 15 September 2020).
[7] R.J. Xie, H.T. Hintzen Ht, Optical properties of (oxy) nitride materials: a review, J. Am. Ceram. Soc. 96 (2013) 665–687.
[8] T.C. Rojas, A. Caro, G. Lozano, J.C. Sánchez-López, High- temperature solar-selective coatings based on Cr(Al)N. Part 1: microstructure and optical properties of CrN_y and $Cr_{1-x}Al_xN_y$ films prepared by DC/HiPIMS, Sol. Energy Mater. Sol. Cells (submitted for publication).
[9] H.C. Barshilia, N. Selvakumar, K.S. Rajam, D.V. Sridhara Rao, K. Muraleedharan, A. Brawas, $TiAlN/TiAlON/Si_3N_4$ tandem absorber for high temperature solar selective applications, Appl. Phys. Lett. 89 (2006) 191909.
[10] H.C. Barshilia, N. Selvakumar, K.S. Rajam, A. Biswas, Optical properties and thermal stability of TiAlN/AlON tandem absorber prepared by reactive DC/RF magnetron sputtering, Sol. Energy Mater. Sol. Cells 92 (2008) 1425–1433.
[11] L. Rebouta, A. Pitaes, M. Andritschky, P. Capela, M.F. Cerqueira, A. Matilainen, K. Pischow, Optical characterization of $TiAlN/TiAlON/SiO_2$ absorber for solar selective applications, Surf. Coating. Technol. 211 (2012) 41–44.
[12] K. Valleti, D.M. Krishna, S.V. Joshi, Functional multi-layer nitride coatings for high temperature solar selective application, Sol. Energy Mater. Sol. Cells 121 (2014) 14–21.
[13] I. Heras, E. Guillén, F. Lungwitz, G. Rincón-Llorente, F. Munnik, E. Schumann, I. Azkona, M. Krause, R. Escobar-Galindo, Design of high-temperature solar-selective coatings based on aluminium titanium oxynitrides $Al_yTi_{1-y}(O_xN_{1-x})$. Part 1: advanced microstructural and optical simulation, Sol. Energy Mater. Sol. Cells 176 (2018) 81–92.
[14] R. Escobar-Galindo, E. Guillén, I. Heras, G. Rincón-Llorente, M. Alcón-Camas, F. Lungwitz, F. Munnik, E. Schumann, I. Azkona, M. Krause, Design of high-temperature solar-selective coatings based on aluminium titanium oxynitrides

$Al_yTi_{1-y}(O_xN_{1-x})$. Part 2: experimental validation and durability tests at high temperature, Sol. Energy Mater. Sol. Cells 185 (2018) 183–191.
[15] A. Rodríguez-Palomo, E. Cespedes, D. Hernández-Pinilla, C. Prieto, High-temperature air-stable solar selective coating based on MoSi2-Si3N4 composite, Sol. Energy Mater. Sol. Cells 174 (2018) 50–55.
[16] A. Al-Rjoub, L. Rebouta, P. Costa, L.G. Vieira, Multi-layer solar selective absorber coatings based on $W/WSiAlN_x/WSiAlO_yN_x/SiAlO_x$ for high temperature applications, Sol. Energy Mater. Sol. Cells 186 (2018) 300–308.
[17] A. Al-Rjoub, L. Rebouta, P. Costa, N.F. Cunha, S. Lanceros-Mendez, N.P. Barradas, E. Alves, The effect of increasing Si content in the absorber layers ($CrAlSiN_x$/$CrAlSiO_yN_x$) of solar selective absorbers upon their selectivity and thermal stability, Appl. Surf. Sci. 481 (2019) 1096–1102.
[18] K. Niranjan, P. Kondaiah, G. Srinivas, H.C. Barshilia, Optimization of W/WAlSiN/SiON/SiO_2 tandem absorber consisting of double layer anti-reflection coating with broadband absorption in the solar spectrum region, Appl. Surf. Sci. 496 (2019) 143651.
[19] X. Wang, T. Luo, Q. Li, X. Cheng, K. Li, High performance aperiodic metal-dielectric multilayer stacks for solar energy thermal conversion, Sol. Energy Mater. Sol. Cells 191 (2019) 372–380.
[20] K. Ibrahim, H. Taha, M. Rahman, H. Kabir, Z. Jiang, Solar selective performance of metal nitride/oxynitride based magnetron sputtered thin film coatings: a comprehensive review, J. Optic. 20 (2018), 033001.
[21] Tables of emittance. http://www.calex.co.uk. (Accessed 15 September 2020). http://www.lumasenseinc.com.
[22] A. Anders, Discharge physics of high power impulse magnetron sputtering, Surf. Coating. Technol. 205 (2011). S1–S9.
[23] D. Lundin, K. Sarakinos, An introduction to thin film processing using high-power impulse magnetron sputtering, J. Mater. Res. 27 (2012) 780–792.
[24] J.A. Duffie, W.A. Beckman, Solar Engineering of Thermal Processes, third ed., John Wiley& Sons, New York, 2005.
[25] E. Standard, N. Europeenne, UNE-EN 673, Determinación del coeficiente de transmisión térmica, Europe, 2011.
[26] ASTM, ASTM G173, Standard Tables for Reference Solar Spectral Irradiance at Air Mass 1.5: Direct Normal and Hemispherical for 37 Degree Tilted Surface, US, 2008.
[27] F. Lungwitz, R. Escobar-Galindo, D. Janke, Erik Schumann, R. Wenisch, S. Gemming, M. Krause, Transparent conductive tantalum doped tin oxide as selectively solar-transmitting coating for high temperature solar thermal applications, Sol. Energy Mater. Sol. Cells 196 (2019) 84–93.
[28] M. Koelhl, Durability of solar energy materials, Renew. Energy 24 (2001) 597–607.
[29] CODE Software for Optical Spectroscopy. WTheiss Hardware and Software https://www.wtheiss.com/(Accessed: 15 September 2020).
[30] T.C. Rojas, S. Domínguez-Meister, M. Brizuela, J.C. Sanchez-Lopez, High-temperature oxidation of CrAlYN coating: implications of the presence of Y and type of steel, Surf. Coating. Technol. 354 (2018) 203–213.
[31] J.C. Sánchez-López, D. Martínez-Martínez, C. López-Cartes, A. Fernández, M. Brizuela, A. García-Luis, J.L. Oñate, Mechanical behaviour and oxidation resistance of Cr(Al)N coatings, J. Vac. Sci. Technol., A 23 (2005) 681–686.
[32] X. Gao, W. Theiss, Y. Qian, P.J. Ma, G. Liu, Optical simulation, corrosion behavior and long term thermal stability of TiC-based spectrally selective solar absorbers, Sol. Energy Mater. Sol. Cells 167 (2017) 150–156.
[33] K.T. Raić, An explanation of hillock growth in thin Al films, Surf. Eng. 32 (11) (2016) 823–828.
[34] C.K. Ho, A.R. Mahoney, A. Ambrosini, M. Bencomo, A. Hall, T.N. Lambert, Characterization of Pyromark 2500 paint for high-temperature solar receivers, J. Sol. Energy Eng. 136 (2014), 014502.
[35] A. Hall, A. Ambrosini, C.K. Ho, Solar selective coatings for concentrating solar power central receivers, Adv. Mater. Process. 170 (1) (2012) 28–32.
[36] H.C. Barshilia, N. Selvakumar, K.S. Rajam, D.V. Sridhara Rao, K. Muraleedharan, TiAlN/TiAlON/Si_3N_4 tandem absorber prepared using reactive direct current magnetron sputtering, Thin Solid Films 516 (2008) 6071–6078.
[37] H.C. Barshilia, K.S. Rajam, Raman spectroscopy studies on the thermal stability of TiN, CrN, TiAlN coatings and nanolayered TiN/CrN, TiAlN/CrN multilayer coatings, J. Mater. Res. 19 (2004) 3196–3205.
[38] J.C. Sánchez-López, A. Contreras, S. Domínguez-Meister, A. García-Luis, M. Brizuela, Tribological behaviour at high temperature of hard CrAlN coatings doped with Y or Zr, Thin Solid Films 550 (2014) 413–420.
[39] T.C. Rojas, S. Domínguez-Meister, M. Brizuela, J.C. Sanchez-Lopez, Influence of Al and Y content on the oxidation resistance of CrAlYN protective coatings for high temperature applications: new insights about the Y role, J. Alloys Compd. 773 (2019) 1172–1181.
[40] J.C. Sánchez-López, A. Caro, G. Alcalá, T.C. Rojas, Tailoring CrN_x Stoichiometry and Functionality by Means of Reactive HiPIMS, Surf. Coating. Technol. 401 (2020) 126235.
[41] M. to Baben, M. Hans, D. Primetzhofer, S. Evertz, H. Ruess, J.M. Schneider, Unprecedented thermal stability of inherently metastable titanium aluminum nitride by point defect engineering, Mater. Res. Lett. 5 (2017) 158–169.